



1 **Observations of the atmospheric boundary layer structure**

2 **over Beijing urban area during air pollution episodes**

3 Linlin Wang<sup>1,2</sup>, Junkai Liu<sup>1,5</sup>, Zhiqiu Gao<sup>1\*</sup>, Yubin Li<sup>2</sup>, Meng Huang<sup>2</sup>, Sihui Fan<sup>2</sup>,  
4 Xiaoye Zhang<sup>3</sup>, Yuanjian Yang<sup>2</sup>, Shiguang Miao<sup>4</sup>, Han Zou<sup>1</sup>, Yele Sun<sup>1</sup>, Yong  
5 Chen<sup>1</sup>, Ting Yang<sup>1</sup>

6 <sup>1</sup>State Key Laboratory of Atmospheric Boundary Layer Physics and Atmospheric Chemistry

7 (LAPC), Institute of Atmospheric Physics, Chinese Academy of Sciences, Beijing 100029, China

8 <sup>2</sup>Collaborative Innovation Centre on Forecast and Evaluation of Meteorological Disasters, School

9 of Atmospheric Physics, Nanjing University of Information Science and Technology, Nanjing,

10 210044, China

11 <sup>3</sup>Chinese Academy of Meteorological Sciences, Beijing, 100081, China

12 <sup>4</sup>Institute of Urban Meteorology, China Meteorological Administration, Beijing, 100081, China

13 <sup>5</sup>University of Chinese Academy of Sciences, Beijing 100049, China

14

15 **Abstract**

16 We investigated the interactions between the air pollutants and the structure of  
17 urban boundary layer (UBL) over Beijing by using the data mainly obtained from the  
18 325-m meteorological tower and a Doppler wind lidar during 1–4 December, 2016.  
19 Results showed that the pollution episodes in this period could be characterized by  
20 low surface pressure, high relative humidity, weak wind, and temperature inversion.  
21 Compared with a clean daytime episode that took place on 1 December, results also  
22 showed that the attenuation ratio of downward shortwave radiation was about 4%, 23%  
23 and 78% at 1200 local standard time (LST) on 2–4 December respectively, while for  
24 the net radiation ( $R_n$ ) attenuation ratio at the 140-m level of the 325-m tower was 2%,  
25 24%, and 86%. The large reduction in  $R_n$  on 4 December was not only the result of the  
26 aerosols, but also clouds. Based on analysis of the surface energy balance at the

---

\*Corresponding author: Dr. Zhiqiu Gao, [zgao@mail.iap.ac.cn](mailto:zgao@mail.iap.ac.cn)



27 140-m level, we found that the sensible heat flux was remarkably diminished during  
28 daytimes on polluted days, and even negative after sunrise (about 0720 LST) till 1400  
29 LST on 4 December. We also found that heat storage in the urban surface layer played  
30 an important role in the exchange of the sensible heat flux. Owing to the  
31 advantages of the wind lidar having superior spatial and temporal resolution, the  
32 vertical velocity variance could capture the evolution of the UBL well. It clearly  
33 showed that weak vertical mixing caused the concentrating of pollutants, and that  
34 vertical mixing would also be weakened by a certain quantity of pollutants, and then  
35 in turn worsened the pollution further. Compared to the clean daytime on 1 December,  
36 the maximums of the boundary layer height (BLH) reduced about 44% and 56% on  
37 2–3 December, when the average  $PM_{2.5}$  ( $PM_1$ ) concentrations in afternoon hours  
38 (from 1200 to 1400 LST) were 44 (48)  $\mu\text{g m}^{-3}$  and 150 (120)  $\mu\text{g m}^{-3}$ . Part of these  
39 reductions of the BLH was also contributed by the effect of the heat storage in the  
40 urban canopy.

41

## 42 **1 Introduction**

43 In recent years, fine particulate matter (PM) pollution events in the atmospheric  
44 boundary layer (ABL), i.e., involving particles with diameters  $\leq 2.5 \mu\text{m}$  ( $PM_{2.5}$ ), have  
45 occurred frequently in urban areas, thus emerging as a serious environmental issue in  
46 China. The Beijing-Tianjin-Hebei (BTH) metroplex region is one of the most  
47 seriously affected areas in China with respect to air pollution. The main hazards or  
48 negative effects of air pollution generally fall into two categories: human health and  
49 transportation. Thus, it is an issue that has attracted considerable public attention and,  
50 accordingly, numerous studies have focused on investigating the sources and  
51 formation mechanisms of air pollution in the BTH region, through numerical  
52 simulation and field observational methods (e.g., Wang et al., 2013; Sun et al., 2014;  
53 Ye et al., 2016; Li et al., 2017; Han et al., 2018).

54 Beijing, the main city of the BTH region, has experienced several high-impact,  
55 persistent, and severe air pollution episodes in recent years, with notable examples



56 having taken place in January 2013, October and November 2014; December 2015  
57 and 2016, and January 2017. Beijing is located on the North China Plain (NCP), and  
58 is surrounded by the Yan and Taihang Mountains from north to west. Therefore,  
59 Beijing is frequently affected by thermally induced mountain-plain wind circulation  
60 over the NCP, which contributes to the transportation of air pollution in Beijing (Liu  
61 et al., 2009; Hu et al., 2014; Chen et al., 2017; Zheng et al., 2018). In addition, it is  
62 well recognized that high levels of anthropogenic emissions and rapid formation of  
63 secondary aerosol are key factors leading to the frequent occurrence of severe haze  
64 episodes (Li et al., 2017). More importantly, these interactions on local and large  
65 scales are associated with the meteorological conditions (Sun et al., 2013; Yang et al.,  
66 2018). Previous studies have reported that heavy pollution in Beijing is highly related  
67 to unfavorable local weather conditions, such as weak wind, strong temperature  
68 inversion, high relative humidity (RH) and low surface pressures (Zhang et al., 2014,  
69 Liu et al., 2017, Li et al., 2018).

70 Many studies have also suggested that the structure of the urban boundary layer  
71 (UBL), in particular wind, turbulence and stability, had strong influences on the  
72 occurrence, maintenance, vertical diffusivity of air pollutants (Han et al., 2009; Zhao  
73 et al., 2013). For instance, emissions of air pollution in urban areas lead to a buildup  
74 of pollutant concentrations due to reduced mixing and dispersion in UBL (Holmes et  
75 al., 2015). An analysis of the dramatic development of a severe air pollution event on  
76 November 2014 in the Beijing area revealed that turbulent mixing played an  
77 important role in transporting the heavily polluted air and PM<sub>2.5</sub> oscillations (Li et al.,  
78 2018). The vertical profiles of wind and temperature along with the BLH are the main  
79 factors affecting turbulence diffusion. Moreover, the BLH is also a key variable in  
80 describing the structure of UBL, and in predicting air-pollution (Stull, 1988; Miao et  
81 al., 2011; Barlage et al., 2016). Miao et al. (2018) found that the concentration of  
82 PM<sub>2.5</sub> anti-correlates with the BLH. In addition, air pollutants also can modulate  
83 radiative transfer processes through the scattering, reflection and absorption of  
84 shortwave radiation and the reflection, absorption and emission of longwave radiation  
85 (Dickerson et al., 1997; Stone et al., 2008; Wang et al., 2014). In response to reduced



86 solar radiation, the cooling of surface air temperature can lead to strong temperature  
87 inversion in the near-surface layer, which can increase the atmospheric stability and  
88 prolong the accumulation of pollution because of the existence of this stable boundary  
89 layer (Barbaro et al., 2013; Che et al., 2014; Gao et al., 2015). A positive feedback  
90 loop in which more aerosol loading leads to a more stable atmospheric boundary layer  
91 (ABL), enhanced accumulation of pollutants within the ABL, and a more polluted and  
92 hazier atmosphere, was described by Zhang et al. (2013; 2018). It is also found that  
93 the further worsened meteorological conditions caused by cumulated aerosol pollution  
94 dormant subsequently occurred "explosive growth" of  $PM_{2.5}$  mass that often appears  
95 in the late stage of heavy aerosol pollution episode in Beijing-Tianjin-Hebei area in  
96 China (Zhong et al., 2017).

97 Although many studies have provided various interesting findings, consensus has  
98 not been reached on the pollutant transport mechanism and the nature of the  
99 interactions between the air pollution and the structure of the UBL, mainly due to a  
100 lack of reliable and detailed field measurements and the complex properties of the  
101 UBL. Additionally, as mentioned above, there are several factors that affect the  
102 occurrence of urban air pollution, which can lead to different pollutant transporting  
103 mechanism characteristics for different pollution events. Therefore, taking a severe  
104 heavy pollution event occurred during 1–4 December, 2016 in Beijing as an example,  
105 we will aim to investigate evolution characteristics of ABL structure and further  
106 explore the interaction between the structure of the UBL and the air pollution by using  
107 the field data collected from a 325-m meteorology tower in Beijing urban area, as  
108 well as from a Doppler wind lidar and a dual-wavelength (1064 and 532 nm)  
109 depolarization lidar. During this pollution episode, the  $PM_{2.5}$  concentration rapidly  
110 increased from about  $100 \mu\text{g m}^{-3}$  to approximately  $500 \mu\text{g m}^{-3}$  at 1200 LST on 4  
111 December, which can be considered as a typical case to achieve a better  
112 understanding the formation, transportation, and dispersion mechanisms of the alike  
113 pollution event, as well as the interactions between the air pollution and the structure  
114 of the UBL.

115 The paper is organized as follows: Section 2 describes the field site, data, and



116 methods. The overall characteristics of the synoptic pattern and the meteorological  
117 factors related to the development of the pollution event are investigated in Section 3.  
118 The impacts of the evolution of the vertical UBL structure on this pollution episode,  
119 and vice versa—especially the turbulence due to the radiative forcing of aerosols—are  
120 also explored in Section 3. Lastly, the results of the study are summarized in Section  
121 4.

## 122 **2 Materials**

### 123 **2.1 Site and data**

124 The main data used in this study were from a tall tower in Beijing, officially known  
125 as “the Beijing 325-m meteorological tower” which is located at an urban site in the  
126 city (39.97°N, 116.37°E; the Beijing “inner-city” site). Within a radius of 5 km of the  
127 tower, buildings of different heights are distributed irregularly in all directions, and  
128 the area is surrounded by four-story to twenty-story buildings with heights of 10 – 60  
129 m (Liu et al., 2017). The surrounding buildings can be seen in Fig.1a. This tall tower  
130 conducts turbulent flux measurements using sonic anemometers (Model Windmaster  
131 Pro, Gill, UK) at three different levels (i.e., 47-m, 140-m and 280-m).  
132 Note that CSAT3 three-dimensional sonic anemometers designed by Campbell  
133 Scientific Inc (USA) at these three levels have been replaced by the Model  
134 Windmaster Pro since 2015, so the turbulence measurements before 2015 used in  
135 previous papers were collected using the CSAT3 sonic anemometers. The new sonic  
136 anemometer experimental setup has been reported by Cheng et al. (2018). Downward-  
137 pointing and upward-pointing pyrgeometers and pyranometers (CNR1, Kipp & Zonen)  
138 are maintained at the same heights as the sonic anemometers to measure  
139 four-component radiation (i.e., incoming shortwave and longwave radiation, and  
140 outgoing shortwave and longwave radiation). Meteorological elements, including  
141 wind speed, wind direction (010C cup anemometers and 020C wind vanes, Metone,  
142 USA), RH and temperature (HC2-S3, Rotronic, Switzerland) are measured at 15  
143 levels (i.e., 8-m, 15-m, 32-m, 47-m, 65-m, 80-m, 100-m, 120-m, 140-m, 160-m,



144 180-m, 200-m, 240-m, 280-m and 320-m) above ground level. An Aerodyne aerosol  
145 chemical speciation monitor and a high-resolution time-of-flight aerosol mass  
146 spectrometer were deployed at 260-m and ground level, repetitively to measure  $PM_{10}$   
147 mass concentrations at 5-min intervals (Sun et al., 2016).

148 In addition, wind speed (05103-L, R. M.Young) and temperature (HMP45C,  
149 Vaisala) at the 2.2-m level are measured at a surface station about 20 m south of the  
150 tower. We also used wind data collected above 100 m by a Doppler wind lidar  
151 (Windcube200, Leosphere, Orsay, France) situated on the rooftop of a 8 m high  
152 building. Furthermore, a dual-wavelength (1064, and 532 nm) depolarization lidar  
153 developed by the National Institute for Environmental Studies, Japan, sits on the  
154 rooftop of a 28 m high building (Yang et al., 2017), which provided us with  
155 information on aerosols at higher layer. The mass concentrations of  $PM_{2.5}$  measured at  
156 the Beijing Olympic Sports Center of the National Air Quality Monitoring Network of  
157 China using Tapered Element Oscillating Microbalance analyzers with hourly  
158 monitored readings, were obtained from the website of China National Environmental  
159 Monitoring Center (<http://113.108.142.147:20035/emcpublish>).

160 The three-dimensional sonic anemometers original records (10 Hz) were  
161 processed, prior to analysis using the methods of double rotation (i.e., yaw and pitch  
162 rotations) and linear detrending. Wang et al. (2014) tested a few averaging periods and  
163 found that a 1-h averaging period is reasonable at this urban site. The processing of  
164 turbulence data in our study followed the method described by Wang et al. (2014).

165 The criterion of threshold carrier-to-noise ratio (CNR) was used to reduce the  
166 effects of invalid data on profiles derived from the Doppler velocities. The data  
167 control process was described in detail by Huang et al. (2017). We calculated the  
168 vertical velocity variance and stream wise wind speed and wind direction over a  
169 30-minute segment.

170 The dual-wavelength depolarization lidar was used to retrieve the aerosol vertical  
171 structure at a spatially resolved resolution of 6 m and temporally resolved resolution  
172 of 10 s, but only for altitudes in excess of 100 m because of an incomplete overlap  
173 between the telescopic field of view and the laser beam. For this study the raw



174 temporal resolution of the retrieved aerosol profiles was set at 30-minute. More  
175 details on the lidar instruments and various data processing techniques were provided  
176 by (Yang et al., 2017).

177 The NCEP FNL (Final) Operational Global Analysis data collected every six  
178 hours, at 0200, 0800, 1400 and 2000 LST, on  $1^\circ \times 1^\circ$  grids was used to analyze the  
179 synoptic-scale weather conditions.

## 180 2.2 Methods

### 181 2.2.1 Turbulent flux and radiation calculation

182 The sensible heat and latent heat fluxes were calculated using the  
183 eddy-covariance method:

$$184 \quad H = \rho C_p \overline{w'T'} \quad (1)$$

$$185 \quad LE = L_v \overline{w'q'} \quad (2)$$

186 where  $u$ ,  $v$ , and  $w$  are the streamwise, cross-stream, and vertical velocities ( $\text{m s}^{-1}$ ),  
187 respectively from the sonic anemometers;  $T$  is the air temperature (K),  $\rho_v$  is the water  
188 vapour density ( $\text{kg m}^{-3}$ ) and  $\rho$  is the air density ( $\text{kg m}^{-3}$ ).  $C_p$  is the specific heat  
189 capacity at constant pressure ( $\text{J kg}^{-1} \text{K}^{-1}$ ).

190 The one-dimensional SEB is usually formulated as

$$191 \quad R_n + Q_F = H + LE + G \quad (3)$$

192 where  $H$  is the sensible heat flux from the surface to the adjacent air,  $LE$  is the latent  
193 heat flux into the atmosphere associated with evapotranspiration, and  $G$  is the ground  
194 and urban canopy heat storage.  $R_n$  is the net radiation, which can be described as

$$195 \quad R_n = DSR - USR + DLR - ULR \quad (4)$$

196  $DSR$  stands for downward shortwave radiation,  $USR$  for upwelling short-wave  
197 radiation,  $DLR$  for downward incoming long-wave radiation, and  $ULR$  for



198 upwelling long-wave radiation.  $Q_F$  is the anthropogenic heat flux which was omitted  
199 here, because of the absence of accurate energy consumption and traffic flow data.  
200 Therefore the heat storage was calculated as  $R_n - H - LE$ .

## 201 **2.2.2 Determination of UBL depths**

202 Lidar techniques have become the most valuable and popular systems to detect  
203 the atmosphere because of their higher spatiotemporal resolution. As a result, many  
204 techniques have been developed to determine the BLH by using the remote sensing  
205 instruments, such as radar wind profilers, aerosol lidars, and ground-based microwave  
206 radiometers (Flamant et al., 1997; Emeis et al., 2004, Haman et al., 2012). Remote  
207 sensing is particularly useful in analyzing vertical profiles of turbulence mixing in  
208 UBL, and is generally easier to deploy than radiosondes (Georgoulas et al., 2009).

209 Recently, the turbulence method to define the BLH has been proposed. The  
210 height of the layer in which vertical velocity variance  $\sigma_w^2$  from the Doppler lidar  
211 exceeds a given threshold is considered as the BLH. Previous investigators have given  
212 different values of  $\sigma_w^2$  for different underlying surfaces (Tucker et al., 2009, Pearson  
213 et al. 2010). Barlow et al. (2011) defined the mixing height as the height over London,  
214 UK up to which  $\sigma_w^2 > 0.1 \text{ m}^2 \text{ s}^{-2}$ . Here, we select this method of Barlow et al. (2011),  
215 because of the similar urban fraction between central Beijing and London.

216 The 30-min vertical velocity standard deviation between lidar is

$$217 \quad \sigma_w = \sqrt{\frac{1}{N-1} \sum_{i=1}^N (w_i - \bar{w})^2} \quad (5)$$

218 Where  $N$  is the record number every 30 minutes,  $w_i$  denotes the  $i$ th vertical velocity  
219 ( $\text{m s}^{-1}$ ), and  $\bar{w}$  is the mean vertical wind speed.

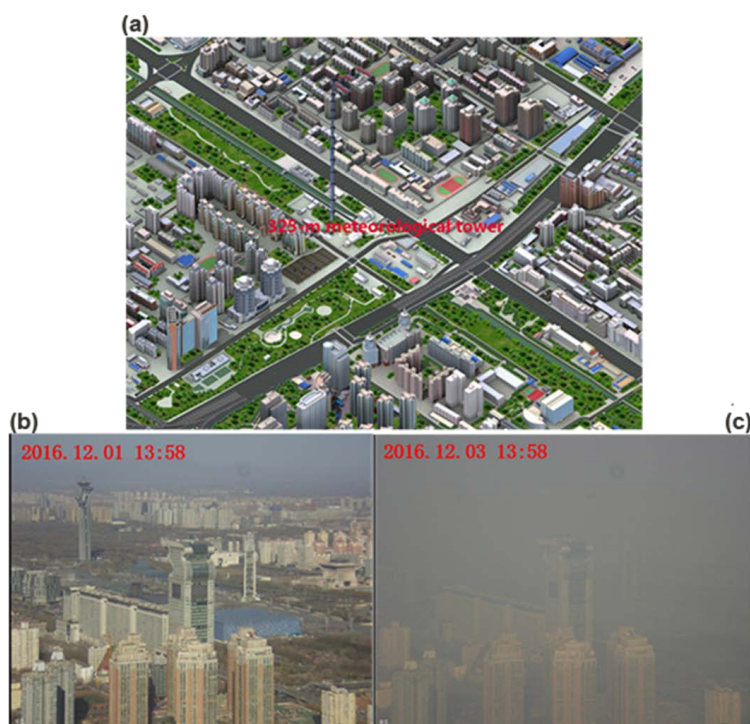
## 220 **3 Results and discussion**

### 221 **3.1 Air pollution episodes in Beijing**

222 As shown in Fig. 1c, the visibility around the 325-m tower at about 1400 LST on  
223 3 December was much lower than that on 1 December. In fact, the visibility decreased

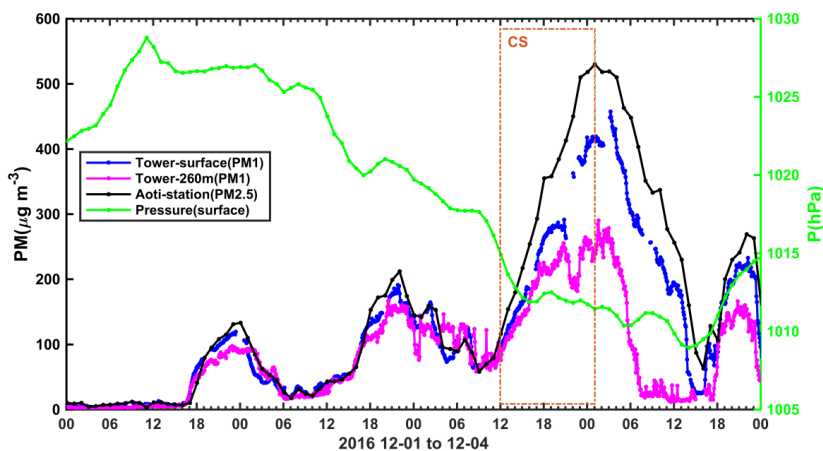


224 rapidly from 1200 to 1600 LST before sunset (1650 LST) on 3 December,  
225 accompanied by the increasing  $\text{PM}_{2.5}$  concentration (from  $100 \mu\text{g m}^{-3}$  to  $200 \mu\text{g m}^{-3}$ )  
226 at the Olympic Sports Center station and  $\text{PM}_1$  concentration (from  $100 \mu\text{g m}^{-3}$  to  $190$   
227  $\mu\text{g m}^{-3}$ ) at the 325-m tower station (Fig. 2). After sunset, the  $\text{PM}_{2.5}$  hourly maximum  
228 concentration reached  $530 \mu\text{g m}^{-3}$  at 0200 LST 4 December. The cumulative  
229 explosive growth process of the pollution, starting at 1200 3 December and lasting till  
230 0200 LST 4 December, is defined as cumulative stage (CS).



231

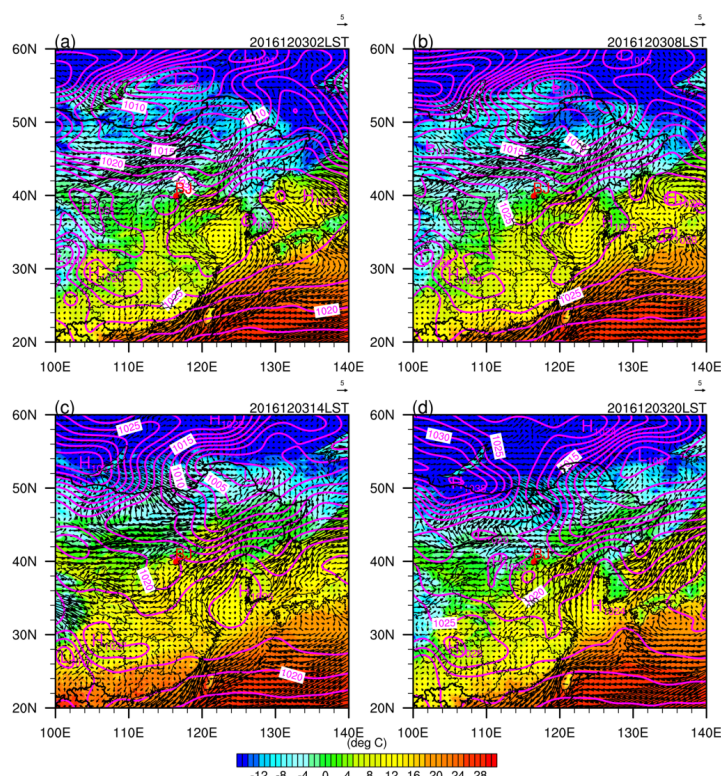
232 **Figure 1: (a) Three-dimensional graph of the underlying surface around the 325-m tower in**233 **Beijing. Photographs of the buildings looking north from the 280-m level of the 325-m tower**234 **at 1358 LST (b) 1 December and (c) 3 December, 2016.**



235

236 **Figure 2: Temporal variation of the PM<sub>1</sub> observed at the surface and the 260-m level of the**  
237 **325-m tower, PM<sub>2.5</sub> at Aoti surface station, and surface pressure at the surface station of the**  
238 **IAP, during 1–4 December 2016. (red box: CS)**

239 The surface pressure measured at the Institute of Atmospheric Physics (IAP)  
240 surface station (Fig. 2) indicated the air quality was getting worse with decreasing  
241 surface pressure. In order to analyze the synoptic background fields for the CS, the  
242 sea level pressure and surface wind field on 3 December are shown in Fig. 3. At 0800  
243 LST, the Beijing region was governed by a saddle type pressure field characterized by  
244 uniform pressure, very weak wind speed and changeable wind direction. The surface  
245 high pressure system over the Bohai and Yellow seas was conducive to the  
246 maintenance of these stagnant meteorological conditions till 1400 LST, which  
247 provided the unfavorable meteorological conditions for the diffusion of air pollutants  
248 and partly led to the CS.



249  
250 **Figure 3: Distribution of surface pressure and temperature at (a) 0200 LST, (b) 0800 LST, (c)**  
251 **1400 LST, and (d) 2000 LST 3 December 2016, where the green star marks the location of**  
252 **Beijing (BJ).**

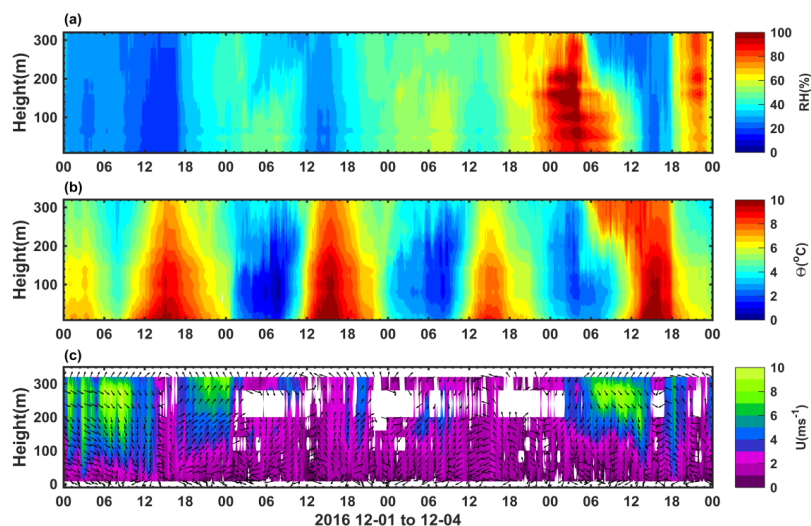
253 Note that, 3 and 4 December were weekend days without vehicle restrictions,  
254 meaning the relatively larger quantities of automobile exhaust were in part  
255 responsible for this heavy pollution process.

### 256 3.2 Meteorological parameters

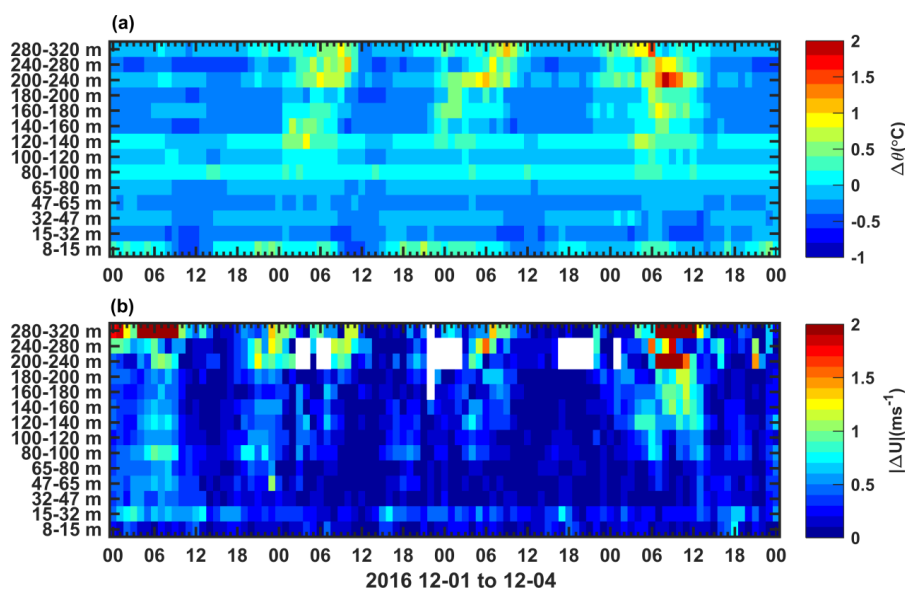
257 As shown in Fig.4a, RH was mostly larger than 40% during pollution episodes,  
258 and increasing along with the concentrated PM<sub>2.5</sub> (PM<sub>1</sub>). Especially during the CS,  
259 RH could reach near to 100% at nighttime, which firstly appeared at the levels of  
260 160–220 m and then extended to the lower levels. Meanwhile, the deeper RH (>80%)  
261 with higher PM concentrations during the CS was possibly caused by secondary  
262 aerosol formation. Due to aerosol cooling force, the  $\theta$  at the daytime on 3 December



263 was much lower than on other days. Temperature inversions were found at all three  
264 nights. Clearly, the wind flow played an important role in the air pollution process.  
265 The Southwesterly wind transported air pollutants from Hebei Province to Beijing on  
266 the first two pollution nights (Fig. 4c). In order to investigate the characteristics of the  
267 UBL structure, the vertical gradients of potential temperature ( $\Delta\theta = \theta_2 - \theta_1$ ) and  
268 gradient absolute values in wind speed ( $|\Delta U| = |U_2 - U_1|$ ) were calculated by  
269 using the adjacent two levels as the thermal and dynamic factors (Fig. 5). It was found  
270 that the vertical gradients of wind speed and potential temperature were small because  
271 of strong vertical thermal mixing during daytime, whereas they were large at  
272 nighttime due to weak vertical mixing. The values of  $\Delta\theta$  and the duration of  $\Delta\theta > 0$   
273 increased day by day, meaning the thermal stability strengthened with worsening  
274 polluted days. A long-term existence of temperature inversion near the surface could  
275 be found till 1200 LST 4 December, associated with extremely steady stability. This  
276 stable surface stratification resulted in the suppressed diffusion of air pollutants at the  
277 surface, causing a dissipation lag for  $PM_{10}$  at the surface compared to the case at the  
278 260-m level (shown in Fig. 2).



279  
280 **Figure 4: Vertical evolution of (a) relative humidity, (b) virtual temperature, and (c) wind**  
281 **speed and wind vectors (arrows), observed at 15 levels of the 325-m tower during 1–4**  
282 **December 2016.**



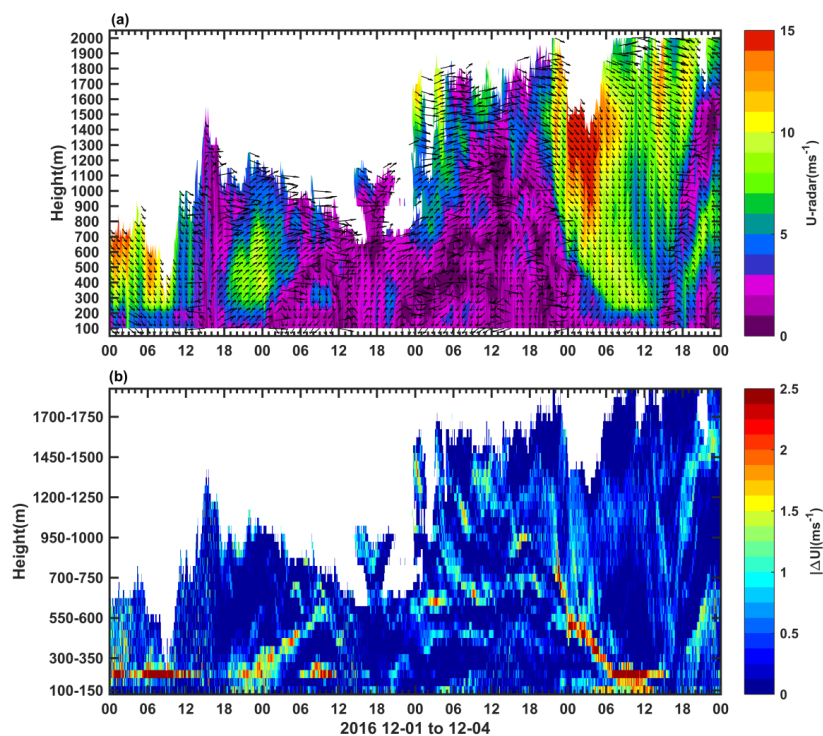
283

284 **Figure 5: Vertical evolution of (a) vertical gradients of relative potential temperature and (b)**  
285 **vertical gradients of zonal wind speed, based on observations at 15 levels of the 325-m tower**  
286 **during 1–4 December 2016.**

287 Owing to the limited height of the tower, the wind profile above several  
288 hundred meters collected by the Doppler lidar (Fig. 6) can be used to further  
289 investigate the association between the wind flow and air pollution process. On 1  
290 December, the air quality was good before noon and there was strong northwest wind  
291 (mostly around  $10 \text{ m s}^{-1}$ ) at 200–1000 m levels above the ground (ATG). In our case,  
292 notably, a low-level jet (LLJ) established after sunset, with the jet core at 300–500 m  
293 ATG, and the maximum wind speed was around  $10 \text{ m s}^{-1}$  at about 2400 LST. We can  
294 see the  $\text{PM}_{2.5} / \text{PM}_{10}$  concentration was starting to increase after sunset with the  
295 maximum  $\text{PM}_{2.5}$  concentration ( $120 \mu\text{g m}^{-3}$ ) observed at 2400 LST, and then  
296 decreased with the gradually weakened LLJ, which suggests this southwesterly LLJ  
297 transferred polluted air from the south by advection to Beijing before midnight. A  
298 previous study also reported that presence of an LLJ can increase the surface pollution  
299 through horizontal advection (Hu et al., 2013). Besides the horizontal advection, LLJ  
300 also can generate vertical mixing due to the wind shear with large  $|\Delta U| (> 1 \text{ ms}^{-1})$ .  
301 Once the northern maintain flow generated, the LLJ became weaker ( $< 5 \text{ ms}^{-1}$ ) in the



302 early morning on 2 December, and then the vertical mixing generated by the  
303 weakened LLJ changed to the dominated term which made an important contribution  
304 to the mixing of the pollutants at the dissipated period. Chen et al. (2018) also pointed  
305 out that a northerly weak LLJ noticeably reduced the PM concentration in urban  
306 Beijing. As a result, the presence of an LLJ has an indispensable effect on the process  
307 of the air pollution in the nocturnal boundary layer (NBL).



308  
309 **Figure 6: Vertical evolution of (a) wind speed and (b) vertical gradients of wind speed, based**  
310 **on Doppler wind lidar observations during 1–4 December 2016.**

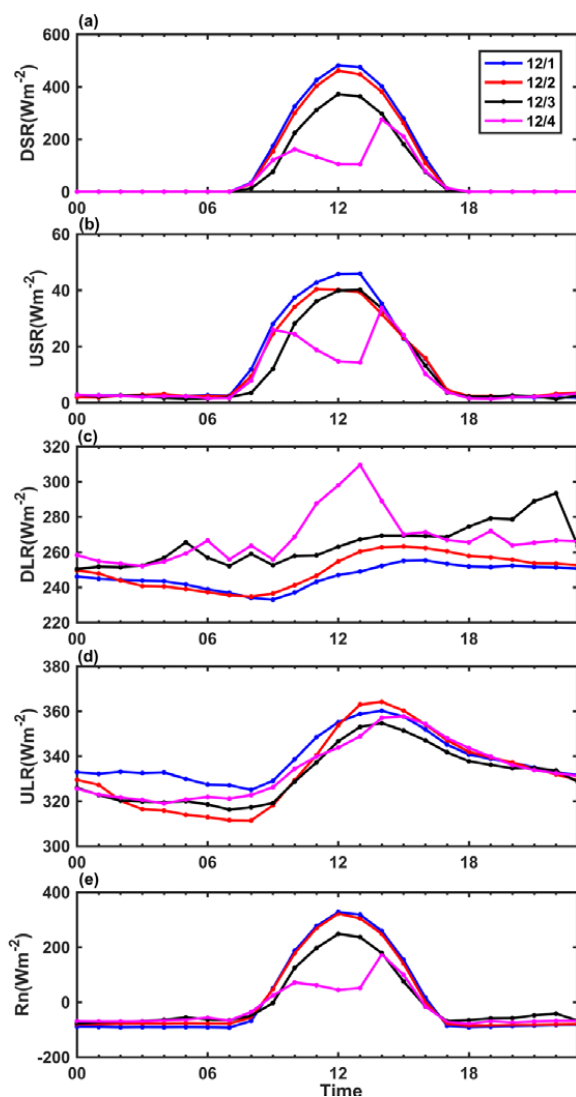
311 We can also see that the  $PM_{10}$  concentration at the 260-m level started to  
312 decrease at 0200 LST 2 December which was about two hours later than  $PM_{10}$  at the  
313 ground level. This could be explained that the gradually deep and clean northwest  
314 mountain-plain wind occurred first below 100 m ATG, and then reached the upper  
315 level. On 2 December, the wind below 1 km was dominated by speeds of around 2 m  
316  $s^{-1}$  from 0600 to 2200 LST. The weak northerly winds did not fully disperse the air  
317 pollutants before the noon. Meanwhile, after the transition time on 1300 LST,



318 southerly winds existed and brought polluted air from the south, and then the air  
319 quality became worsened, and the maximum  $PM_{2.5}$  concentration ( $210 \mu\text{g m}^{-3}$ )  
320 occurred at 2200 LST. Compared to early morning on 2 December, the wind below  
321 600 m was weaker and the vertical gradients (Fig. 6b) were much smaller, meaning  
322 mechanical turbulence (vertical mixing) was extremely weak. Thus, there is no  
323 dramatic reduction in the air pollution before sunrise on 3 December, and then the CS  
324 began at noon when the wind speeds were mostly lower than  $3 \text{ m s}^{-1}$  below 1 km ATG,  
325 because of the saddle-type pressure-field background (Fig. 3).

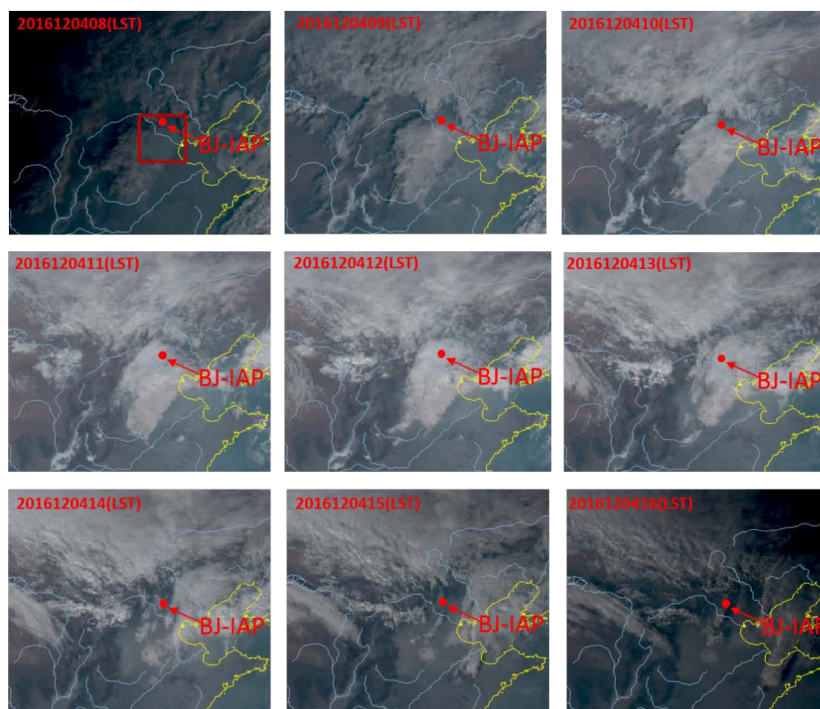
### 326 **3.3 SEB characteristics**

327 Radiation from the sun is the most important driver of the development of the  
328 UBL. Various climatic changes within urban ABL are driven by the SEB, which  
329 distributes the energy by radiation, convection and conduction between a facet (Oke et  
330 al., 2017). Therefore, the SEB, described as Eq. 3, is a fundamental aspect  
331 contributing to our understanding of the variations in the UBL.



332

333 **Figure 7: Diurnal cycle of (a) downward shortwave radiation, (b) upward shortwave**  
334 **radiation, (c) downward longwave radiation, (d) upward longwave radiation, and (e) net**  
335 **radiation, observed at the 140-m level of the 325-m tower during 1–4 December 2016.**



336

337 **Figure 8: Hourly Himawari-8 geostationary meteorological satellite cloud images from 0800**  
338 **LST to 1600 LST 4 December, where the red point marked the location of IAP station in**  
339 **Beijing, and the red square marked the mass of grey.**

340 In this study, we wanted to focus on the SEB at one level rather than the vertical  
341 difference at between different levels. Moreover, measurements at the 140-m are  
342 above the roughness sublayer layer and are within the surface layer (Miao et al. 2012),  
343 hence only the observations at the 140-m level were used in studying the radiative  
344 exchange. In Fig. 7, the four components shows the daytime pollution received less  
345 shortwave radiation but more longwave radiation than the daytime clean episode. The  
346 *DSR* reduces with gradually worsening air quality on a day-to-day basis. The *DSR*  
347 during this 4-day period reached a peak value ( $482 \text{ W m}^{-2}$ ) at 1200 LST 1 December.  
348 The differences between the daytime clean and pollution episodes reached about 20  
349 and  $110 \text{ W m}^{-2}$  at 1200 LST on 2 and 3 December. On 4 December, the largest  
350 difference was  $376 \text{ W m}^{-2}$  at 1200 LST, followed by 1400 LST ( $127 \text{ W m}^{-2}$ ), which  
351 approximates that at 1400 LST on 3 December ( $105 \text{ W m}^{-2}$ ). Overall, compared with  
352 the *DSR* during the daytime clean episode on 1 December, the attenuation ratio of the

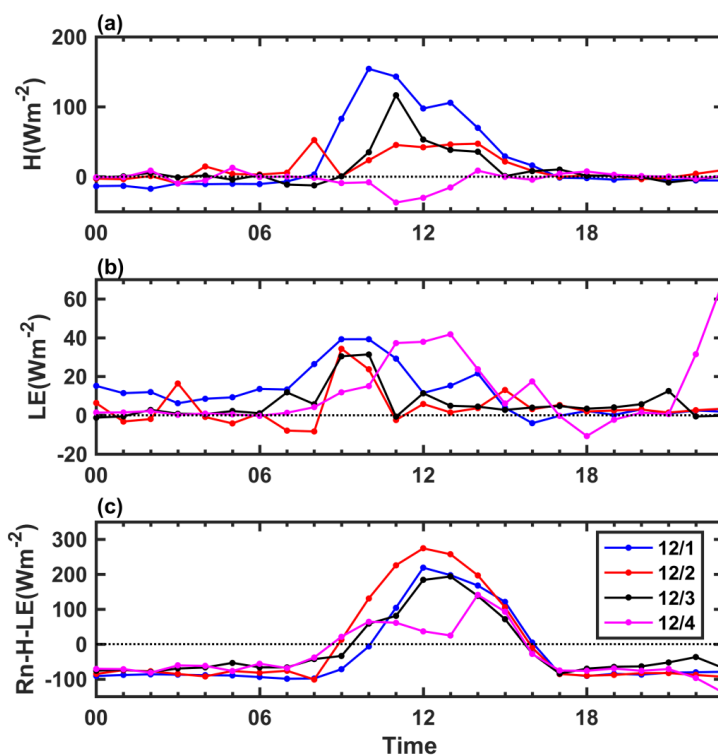


353 *DSR* was about 4%, 23% and 78% at 1200 LST 3–4 December, respectively. Many  
354 efforts have been made on the radiative forcing due to the increasing aerosols loading  
355 by using model simulations and field experiments (Ramanathan et al., 2001; Xia et al.  
356 2007; Ding et al., 2016). Based on observations at the 140-m level at 325-m tower  
357 under eight cloudless days (three clean days and five pollution days) in January 2015,  
358 Wang et al. (2016) found that the maximum attenuation of the *DSR* was  $33.7 \text{ W m}^{-2}$   
359 and the attenuation ratio was 7.4% at 1200 LST. Due to the difference in solar angle,  
360 degree of pollution, pollutant component, cloud etc., attenuation differences are  
361 expected in different case studies. Here, the *USR* on clean days was larger than in  
362 pollution days with a larger maximum difference ( $32 \text{ W m}^{-2}$ ) on 4 December, which  
363 was mainly caused by the lower quantity of *DSR* received on 4 December. For the  
364 *DLR*, the diurnal change in the difference between 1 December and 2 December was  
365 insignificant. During the other two daytimes, the *DLR* increased with the  
366 enhancement of pollution level, and the peak values on 3 December and 4 December  
367 were respectively  $51 \text{ W m}^{-2}$  and  $56 \text{ W m}^{-2}$ .

368 The diurnal variation of the *DSR* on December 4 was discontinuous, which  
369 suggests the large attenuation of the *DSR* on this day was not only the impact of the  
370 higher aerosol concentrations, but also that of the cloud cover. The largest *DLR* on 4  
371 December also indicated the possibility existence of clouds. Information on the  
372 coverage of clouds can be seen from satellite cloud images, which in this case were  
373 provided by the products of the Himawari-8 geostationary meteorological satellite,  
374 launched by the Japan Meteorological Agency (<http://www.eorc.jaxa.jp/ptree/>).  
375 According to these data, the first three days were free from clouds (figures are  
376 omitted). From the mass of grey marked by the red square in Fig. 8, it is apparent that  
377 pollutants dominated the BTH region at 0800 LST, and then this area became partially  
378 cloudy. The area over Beijing was covered with cloud at 1000 LST, which lasted  
379 about 3 hours, and then at 1500 LST had become cloudless. Van de Heever and  
380 Cotton (2007) found giant nuclei could lead to strong early enhancement of cloud  
381 development. Moreover, previous studies have found that cloud fraction changes with  
382 aerosol loading (Gunthe et al., 2011; Che et al., 2016). In our case, before the cloudy



383 day, heavy pollutants occurred over the BTH region, and the IAP station recorded  
384 high relative humidity (> 90%, shown in Fig.4) at midnight, which would have  
385 enhanced aerosol hygroscopic growth, implying significant aerosol–cloud interactions,  
386 referred to Che et al. (2016). Thus, we can deduce that the cloud cover over the BTH  
387 region may in part account for the aerosols on the pollution days, which supports the  
388 abundant cloud condensation nuclei (CCN) for the cloud formation on the following  
389 day. Certainly, further studies with more measurements data and model simulations  
390 are needed to validate this conclusion.  
391



392  
393 **Figure 9: Diurnal cycle of (a) sensible heat flux, (b) latent heat flux, and (c) heat storage**  
394 **(termed as  $R_n - H - LE$ ), observed at the 140-m level of the 325-m tower during 1–4**  
395 **December 2016.**

396 In general, the  $R_n$  (shown in Fig. 7) attenuation ratio was 2%, 24%, and 86%,  
397 respectively, at 1200 LST 2–4 December. This attenuation of the radiation in pollution  
398 days directly resulted in the change of the SEB, and further induced the change in



399 structure of the UBL. In Fig. 9, clearly,  $LE$  was extremely low, at less than  $50 \text{ W m}^{-2}$   
400 during this 4-day period in winter over the large impervious urban surfaces of Beijing.  
401 The fraction of impervious surfaces around the tower was investigated using an  
402 analytical footprint model and found to exceed 65% (Wang et al., 2015). Mostly,  
403 during daytime, the heat storage was the largest consuming term in the SEB,  
404 accounting for about 65 %, 83 %, 78 % and 71 % averaged in the afternoon hours  
405 (1200–1400 LST) on 1–4 December, respectively. During the early morning on 2  
406 December, the air temperature near the surface (illustrated in Fig. 4) was lower than  
407 on other mornings (i.e., at around 0400 LST, about  $5^\circ\text{C}$  lower than on 1 December at  
408 2-m level ABG) and dropped to around zero, meaning a large amount of heat was lost  
409 from the urban volume. Then after sunrise, due to the high thermal conductivity of the  
410 concrete (about 65 times as large as the air), a considerable part of the  $R_n$  (maximum  
411 reaching 85% at 1200 LST) was balanced by the heat storage in the urban fabric.  
412 Compared with 1 December, the larger heat storage with similar  $R_n$  (differing by less  
413 than  $16 \text{ W m}^{-2}$ ) on 2 December led to weaker heat flux, which was negative to the  
414 evolution of UBL and the diffusion of the pollutants, with a slight increasing tend  
415 from 0900 LST to noon, (illustrated in Fig. 2). Specifically, under the conditions of  
416 early morning, much more solar heat is absorbed to warm the large urban fabric after  
417 sunrise, besides, momentum transfer is weak, which leads to less sensible heat. Thus,  
418 in this case, the greater role played by the heat storage in the SEB on pollution days  
419 was responsible for the weakened evolution of the convective boundary layer (CBL).  
420 Compared with the rural surface, Kotthaus and Grimmond (2014) reported the heat  
421 storage in urban surfaces led to delayed warming/cooling, which resulted in the  
422 nocturnal stable conditions generally developing later (Barlow et al., 2015). In our  
423 study, over the urban surface, depending on the differing colder (warmer) early  
424 mornings, heat storage therefore caused a weaker (stronger) development of the CBL.

425 The peak value of the  $H$  was about  $154 \text{ W m}^{-2}$ ,  $53 \text{ W m}^{-2}$ , and  $117 \text{ W m}^{-2}$ , on 1–  
426 3 December, respectively. On 3 December, the heat flux showed a dramatically  
427 decrease, e.g. from  $117 \text{ W m}^{-2}$  to  $53 \text{ W m}^{-2}$  in one hour (1100–1200 LST), which  
428 aggravated the negative effect on pollutants diffusion (corresponding to the CS).



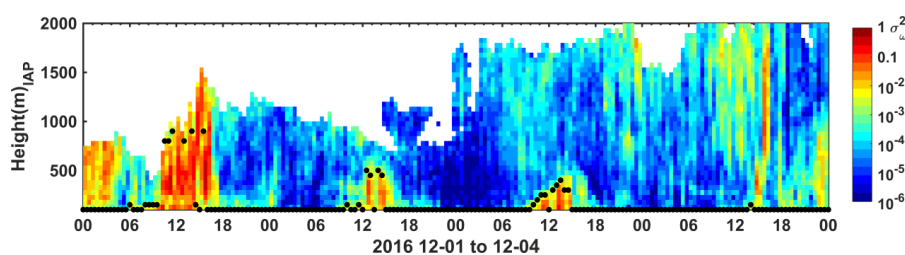
429 There was a thick temperature inversion near to the surface that lasted till the  
430 afternoon on 4 December, as described in last section, which resulted in the  
431 downward heat transfer ( $H < 0$ ) to the urban surface in daytime. Gao et al. (2015) also  
432 found that large positive radiative forcing reduced the  $H$  and  $LE$  by  $5\text{--}16 \text{ W m}^{-2}$  and  
433  $1\text{--}5 \text{ W m}^{-2}$  during a severe fog-haze event over the NCP, by using WRF-Chem  
434 model simulations. By analyzing the measurements collected at a rural site (farmland)  
435 Gucheng in Hebei Province from 1 December 2016 to 31 January 2017 in winter, Liu  
436 et al. (2018) confirmed that the mean daily maximum  $H$  was only  $40 \text{ W m}^{-2}$  on  
437 heavily polluted days (daily mean  $\text{PM}_{2.5}$  concentration  $> 150 \mu\text{g m}^{-3}$ ), but reached  $90$   
438  $\text{W m}^{-2}$  on clean days (daily mean  $\text{PM}_{2.5}$  concentration  $< 75 \mu\text{g m}^{-3}$ ). In our case, in  
439 addition to the influence of heat storage in the urban canopy, the large reductions of  $H$   
440 on 2–4 December also imply that the high  $\text{PM}_{2.5}$  ( $\text{PM}_1$ ) concentrations from the  
441 nighttime till after sunrise may have caused a fatal influence on the evolution of the  
442 UBL. To improve our understanding of the role of the SEB in air pollution process,  
443 more work is needed, such as consideration of anthropogenic heat flux and the  
444 uncertainty in eddy-covariance observations over complex heterogeneous urban  
445 surfaces. Model simulations have pointed out that the reduced sensible heat resulting  
446 from aerosol backscattering could lower the air temperature and suppress the growth  
447 of the ABL (Yu et al. 2002). Therefore, further and more detailed investigation into  
448 the development of the UBL was reported in the next section.

### 449 **3.4 Development of the UBL**

450 The diurnal cycle of the ABL exerts strong control on the scalar concentrations  
451 of air pollutants (Oke et al., 2017). It is known that the ABL starts to grow after  
452 sunrise, and deepens to a maximum value in mid-afternoon; the whole layer is  
453 convectively unstable and well mixed during daytime, in which layer is defined  
454 as CBL, and this part of the atmosphere is directly affected by solar heating of the  
455 surface. After sunset, accompanied by diminishing turbulence, the boundary-layer  
456 depth declines rapidly, and then the boundary layer becomes to the NBL. Based on the  
457 general changes in BLH, the TKE at a certain depth or the amount of solar radiation,



458 previous studies have proven that vertical mixing affects pollutants diffusion (Guinot  
459 et al., 2006; Sun et al., 2013; Guo et al., 2017). However, few have documented the  
460 diurnal circle of the intensity variation of vertical mixing in the UBL, on account of  
461 the limitation of instruments. Here, we took advantages of the Doppler lidar (superior  
462 spatial and temporal resolution), to quantify the values of the vertical mixing,  
463 described as vertical velocity variance  $\sigma_w^2$  on clean and polluted days.



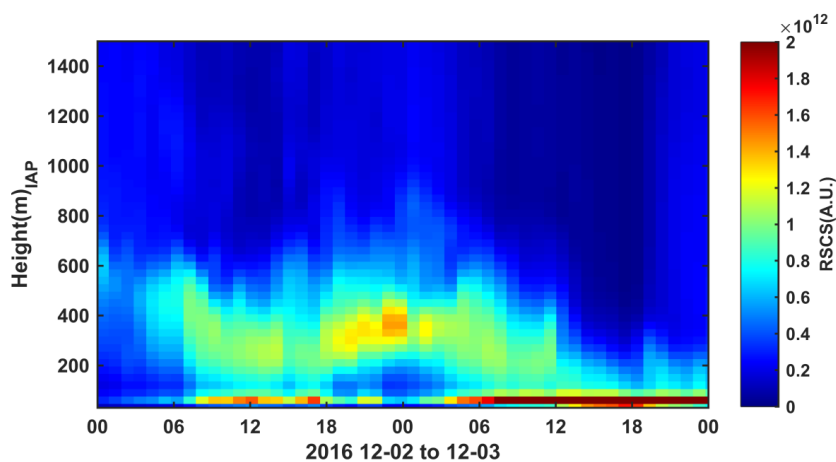
464  
465 **Figure 10: Velocity variance,  $\sigma_w^2$  ( $\text{m}^2 \text{s}^{-2}$ ), calculated from the Doppler wind lidar data.**  
466 **Derived planetary boundary layer depths, based on the threshold method, are depicted as**  
467 **black dots.**

468 As presented in Fig. 10, it was found that the variance of  $\sigma_w^2$  could characterize  
469 the development of the UBL.  $\sigma_w^2$  became greater after sunrise (0720 LST), then  
470 reached a maximum at about 1400 LST, exhibiting an obvious trend of decline  
471 (from  $\sigma_w^2 > 10^{-1}$  to  $\sigma_w^2 < 10^{-2} \text{ m}^2 \text{ s}^{-2}$ ) after sunset (1650 LST). When the UBL developed  
472 into NBL,  $\sigma_w^2$  was about  $10^{-3} \text{ m}^2 \text{ s}^{-2}$  at the 200–300 m levels till midnight and  
473 decreased to about  $10^{-4} \text{ m}^2 \text{ s}^{-2}$  after midnight until sunset.  $\sigma_w^2$  was obviously lower  
474 and its vertical distribution shallower during daytime pollution episodes compared  
475 with the daytime clean episode. On 4 December, the vertical mixing was very weak,  
476 ranging from  $10^{-4}$  to  $10^{-5}$ , and there was barely any diurnal variation of  $\sigma_w^2$  till 1500  
477 LST when the  $\text{PM}_{2.5}$  ( $\text{PM}_{10}$ ) had completely dissipated, which suggests the  
478 radiative cooling of pollutants was a major factor of influence in the UBL  
479 development by suppressing vertical mixing. In return, the stagnating UBL seemed to  
480 act an umbrella, blocking the entrainment with cold-clean air at the upper level, and  
481 solar radiation to the surface, and then further suppressing the diffusion of pollutants,  
482 leading to the increasing  $\text{PM}_{2.5}$  ( $\text{PM}_{10}$ ) concentration during the CS and much slower  
483 diffusion of  $\text{PM}_{10}$  at the surface than that at the 260-m level (Fig. 2). Accordingly, in



484 our case study, this two-way feedback mechanism between air pollutants and the UBL  
485 is strikingly responsible for the cumulative and dissipation stage of these pollution  
486 episodes in our case.

487 Compared to 1 December, the vertical mixing is weaker till about 5 hours after  
488 the sunrise on 2 December (CS). This weak evolution of the CBL was consistent with  
489 the weak sensible heat flux (Fig. 9). As discussed in Section 3.3, a large amount of the  
490 heat was trapped in the cold urban fabrics, resulting in poor sensible heat flux after  
491 sunrise on 2 December.



492  
493 **Figure 11: Evolution of the lidar range-squared-corrected signal (RSCS) at 532 nm from**  
494 **1200 LST 2 December to 1200 LST 3 December 2016. The color scale indicates the intensity**  
495 **of the RSCS, and warm colors represent stronger light scattering.**

496 Additionally, the  $\sigma_w^2$  was mainly ranged from  $10^{-6}$  to  $10^{-5}$   $\text{m}^2 \text{s}^{-1}$  ATG to the  
497 detectable observing height during the nighttime from 2200 LST 2 December till the  
498 early morning 0500 LST before the CS on 3 December. This ultra-weak turbulence  
499 transport maintained a very shallow and stable NBL. Note that values of the  $\text{PM}_{10}$   
500 concentration (Fig.2) at the 260-m height of the 325-m tower  
501 changed slightly with the time during the ultra-weak turbulence transport periods.  
502 Moreover, before the CS on 3 December, the aerosol lidar data (Fig. 11) showed that  
503 the gradient of the range-squared-corrected signals (RSCS) between the levels of  
504 200–250 m and 400–500 m ATG were larger than the other levels from 1800 LST  
505 (after sunset) 2 December to 0500 LST (before sunrise) 3 December. As we know,



506 both aerosols and water vapor affect the signals of the lidar. The larger RSCS at the  
507 time mentioned above, in our case, must not only have been because of the water  
508 vapor but also aerosol concentrations, being consistent with the larger PM<sub>1</sub>  
509 concentration at the 260-m level (more than 100  $\mu\text{g m}^{-3}$ ). Similarly, the larger RSCS  
510 between the levels of 200–250 m and 400–500 m ATG illustrated these levels were  
511 accumulated with high levels of pollutants and the vertical distribution of pollutants  
512 was inhomogeneous, all of which implies that the 260-m level may have been in the  
513 residual layer. The pollutants in the residual layer are known to play an important role  
514 in the diurnal changes of pollutants at the surface (Hastie et al., 1993; Berkowitz et al.,  
515 2000; Salmond and Mckendary, 2006). Sun et al. (2013) suggested that the high  
516 concentration of particles in the residual layer could reach the ground the following  
517 morning through convection, causing severe pollutant concentrations in Beijing. In  
518 the Tianjin area, Han et al. (2018) also found that a pollution layer was present at the  
519 altitude of 1000 m in the early morning on 16 December, 2016, where the aerosols in  
520 the higher layers were transmitted to the ground by downward flow before the  
521 formation of heavy pollution. Actually, many studies have focused on this mechanism  
522 of pollutant vertical mixing in a stable NBL from the micrometeorology perspective.  
523 Turbulence in a very stable NBL is typically intermittent and generated by mechanical  
524 shear associated with changes in wind velocity with height (Mahrt et al., 1998),  
525 referred to as upside-down turbulence in an upside-down boundary structure,  
526 compared to the convective daytime case (Mahrt, 1999; Mahrt and Vickers, 2002).  
527 This upside-down structure is characterized by TKE (or  $\sigma_w^2$ ) and turbulent fluxes  
528 increasing with height, and negative transportation of TKE or velocity variances  
529 (Banta et al., 2006). As shown in Fig. 10, the  $\sigma_w^2$  became larger at lower levels from  
530 0500 LST 3 December, and then the largest values of  $\sigma_w^2$  existed at the 500–600 m,  
531 along with the corresponding  $|\Delta U|$  shown in Fig. 6b. This turbulence could transport  
532 the pollutants accumulated in the residual layer downward to the lower levels, and  
533 contributed to the later CS of the pollution. Halios and Barlow (2018) also suggested  
534 that shear production dominates in the upper half of the UBL, and could therefore not  
535 be neglected, even in cases with low wind. Consequently, the intermittent turbulence



536 generated by the wind shear above a stable UBL plays an important role in the vertical  
537 spreading of pollutants.

538 As a key variable describing the structure of the UBL, the urban BLH estimated  
539 using the threshold method ( $\sigma_w^2 > 0.1 \text{ m}^2 \text{ s}^{-2}$ ) from the Doppler lidar data is also  
540 shown in Fig. 10. For the CBL, the diurnal variations of CBL height were not  
541 described well by the threshold method for these 4-day, and especially on 4 December  
542 for the weak turbulence on polluted day. Eventually, this empirical method was  
543 derived using data in autumn or summer, during which the vertical turbulence is much  
544 greater than in the winter. In our study, the criterion  $\sigma_w^2 > 0.1 \text{ m}^2 \text{ s}^{-2}$  was not  
545 applicable because of weak vertical turbulence transport ( $\sigma_w^2 < 0.1 \text{ m}^2 \text{ s}^{-2}$ ) at certain  
546 times of the day. The threshold method was also invalid in the NBL during this study  
547 period. This may be because of the weak vertical turbulence or smaller height of the  
548 NBL falling below the observable height (100 m). Using Windcube100 data during  
549 summer in Beijing, Huang et al. (2017) also pointed that this method was reasonable  
550 for estimating the CBL depth, while it failed to determine the planetary boundary  
551 layer depths for late-night. Subsequently, they defined the NBL top as the height at  
552 which the vertical velocity variance decreases to 10 % of its near-surface maximum  
553 minus a background variance. However, this new method for the depth of the NBL  
554 also failed in our studied period (figure omitted). This is because the NBL in winter is  
555 mostly steady, which does not satisfy the near-neutral assumption for the method  
556 developed by Huang et al. (2017). Additionally, the NBL has been a major problem  
557 for meteorologists for a long time, especially over polluted urban canopies, which  
558 make the problem far more complex. Therefore, further investigation of this method  
559 should be made in future.

560 Miao et al. (2018) pointed out that the BLH of a fully developed CBL was  
561 clearly anti-correlated with the daily  $\text{PM}_{2.5}$  concentration, implying that the change in  
562 the BLH in the afternoon plays an important role in pollution levels, which is similar  
563 with our present. Furthermore, the mixing heights of the fully coupled CBL for 1–,  
564 December were about 900 m, 500 m, and 400 m, respectively. Due to the weaker  
565 mixing intensity on 4 December, it is difficult to capture specific values of the BLH.



566 As shown in Fig. 2, the maximum daily  $PM_{2.5}$  ( $PM_1$ ) concentrations increased  
567 day-by-day from 1 to 3 December, indicating high pollutants concentration near the  
568 surface coincide with a shallow CBL. Petäjä et al. (2016) reported that aerosol–  
569 boundary layer feedback remained moderate at fine PM concentrations lower than  
570  $200 \mu\text{g m}^{-3}$  in Nanjing area, but became intensive at higher PM loadings, and the  
571 BLH reduced to half of the original height at particle mass concentrations slightly  
572 above  $200 \mu\text{g m}^{-3}$ . Similarly, particularly strong interactions were verified in the  
573 Beijing area when the  $PM_{2.5}$  mass concentration was larger than  $150\text{--}200 \mu\text{g m}^{-3}$   
574 (Luan et al., 2018). In our investigation, the low  $PM_{2.5}$  ( $PM_1$ ) concentration  $46$  ( $48$ )  $\mu\text{g}$   
575  $\text{m}^{-3}$  with a 5% attenuation of  $R_n$  reduced the BLH by about 44% on 2 December.  
576 Additionally, for the  $PM_{2.5}$  ( $PM_1$ ) concentration of  $180$  ( $150$ )  $\mu\text{g m}^{-3}$  on 3 December, a  
577 56% reduction was found with a 25% attenuation of  $R_n$ . In addition to the  $R_n$  term, it  
578 is important to note that the heat storage term in the SEB also makes a significant  
579 contribution to reducing the BLH (details discussed in Section 3.3).

## 580 4 Conclusion

581 Using data from the 325-m meteorological tower in Beijing and two nearby  
582 lidars, we investigated the characteristics of UBL structure during 1–4 December,  
583 2016 in Beijing and examined the interaction between the structure of the UBL and  
584 the air pollution during three pollution episodes, especially the rapid CS during which  
585 the  $PM_{2.5}$  concentration rose from about  $100 \mu\text{g m}^{-3}$  to  $500 \mu\text{g m}^{-3}$  in 12 hours. The  
586 main conclusions can be summarized as follows.

587 1) During this 4-day study period, the air pollution gradually worsened on a  
588 day-by-day basis, with decreasing surface air pressure. Specially, the large-scale  
589 circulation with a saddled pressure field was highly unfavorable for the dispersion of  
590 pollutants on 3 December during the CS. The RH was larger than 40% during the  
591 pollution episodes, and the vertical distribution of RH showed a remarkably  
592 inhomogeneous pattern during the peak period of the CS with the deep RH ( $> 80\%$ ) at  
593 the 47–240-m levels and heavy surface  $PM_{2.5}/PM_1$  concentration (about  $500 \mu\text{g}$   
594  $\text{m}^{-3}/400 \mu\text{g m}^{-3}$ ) in the early morning on 4 December. Temperature inversion ( $\Delta\theta > 0$ )



595 occurred during all three nights. For the first pollution episode during the nighttime on  
596 1-2 December, a southern neutral LLJ was found at the 200–1000-m levels after  
597 sunset till midnight over Beijing, which transported the pollutants from the south of  
598 Beijing by advection. For the second episode during nighttime on 2–3 December,  
599 weak southerly wind ( $<3 \text{ m s}^{-1}$ ) dominated below 600-m level, with small vertical  
600 gradients. Meanwhile, for CS on 3 December, there was a very deep and weak wind  
601 layer, which extended to about 1100-m level till 2200 LST 3 December, when the  
602 accumulated  $\text{PM}_{2.5}$  concentration was larger than  $400 \mu\text{g m}^{-3}$  at the surface.

603 2) Compared with the *DSR* during the daytime clean episode on 1 December, the  
604 attenuation ratio of the *DSR* was about 4%, 23% and 78%, respectively, at 1200 LST  
605 2–4 December, which mainly caused a 2%, 24% and 86% reduction of the  $R_n$ . The  
606 large attenuation of solar radiation on 4 December resulted from the cloud caused by  
607 the large aerosol loading with high RH on 3 December, possibly supporting plentiful  
608 CNN for the formation of cloud. Generally, the latent heat exchange term was very  
609 low during these four days over the urban canopy in Beijing, and the dominate term  
610 was mostly the heat storage, calculated as  $R_n - H - LE$ , during daytime, which  
611 accounted for about 65%, 83%, 78% and 71% of  $R_n$  (averaged 1200–1400 LST) on 1–  
612 4 December, respectively. We also found that the lower  $H$  appeared on the polluted  
613 days than on the clean days, which partly caused by the large consuming term of the  
614 heat storage in the urban fabric.

615 3) In the CBL, the diurnal circle of lidar-based  $\sigma_w^2$  agreed with the variation of  
616 the diurnal cycle of  $H$  estimated by the eddy-covariance method at the 140-m level of  
617 the 325-m tower, showing that vertical mixing was obviously weakened on polluted  
618 days. Compared to the clean day, the evolution of the UBL was delayed by about 5  
619 hours after sunrise (about 0720 LST) on 4 December, because of the long-term ( $> 12$   
620 hours) existence of temperature inversion resulting from the effects of both aerosols  
621 and clouds. This stagnating UBL seemed to act like an umbrella, suppressing the  
622 diffusion of  $\text{PM}_1$  at the surface, which was cleaned at about 1500 LST, while the  $\text{PM}_1$   
623 at the 260-m level was cleaned by the strong clean northerly wind flow at about 0700  
624 LST. Therefore, this two-way feedback mechanism between air pollutants and the



625 UBL was strikingly responsible for the cumulative and dissipation stage of this  
626 pollution event in our case. Additionally, the intermittent turbulence generated by the  
627 wind shear above the stable NBL in the early morning on 3 December may have  
628 contributed to the CS through the downward transporting pollutants from the residual  
629 layer. Compared to 1 December the reduction of the maximum BLH was 44% on 2  
630 December and 56% on 3 December, whereas, the BLH on 4 December was  
631 unobtainable due to the stagnating UBL growth.

### 632 **Acknowledgements**

633 This work was funded by the National Key Research and Development Program of  
634 the Ministry of Science and Technology of China (2016YFC0203304 and  
635 2017YFC0209601).

### 636 **References**

- 637 Banta, R. M., Pichugina, Y. L., and Brewer, W. A.: Turbulent velocity-variance  
638 profiles in the stable boundary layer generated by a nocturnal low-level Jet, *J. Atmos.*  
639 *Sci.*, 63, 2700-2719, 10.1175/JAS3776.1, 2006.
- 640 Barbaro, E., Vilà-Guerau de Arellano, J., Krol, M. C., and Holtslag, A. A. M.: Impacts  
641 of aerosol shortwave radiation absorption on the dynamics of an idealized convective  
642 atmospheric boundary layer, *Boundary-Layer Meteorol.*, 148, 31-49,  
643 10.1007/s10546-013-9800-7, 2013.
- 644 Barlage, M., Miao, S. G., and Chen, F.: Impact of physics parameterizations on  
645 high-resolution weather prediction over two Chinese megacities, *J. Geophys. Res.*,  
646 121, 10.1002/. 2016.
- 647 Barlow, J. F., Halios, C. H., Lane, S. E., and Wood, C. R.: Observations of urban  
648 boundary layer structure during a strong urban heat island event, *Environ. Fluid*  
649 *Mech.*, 15, 373-398, 10.1007/s10652-014-9335-6, 2014.
- 650 Berkowitz, C. M., Fast, J. D., and Easter, R. C.: Boundary layer vertical exchange  
651 processes and the mass budget of ozone: Observations and model results, *J. Geophys.*  
652 *Res.*, 105, 14789-14805, 10.1029/2000jd900026, 2000.
- 653 Bowen, B. M., Baars, J. A., and Stone, G. L.: Nocturnal wind direction shear and its  
654 potential impact on pollutant transport, *J. Appl. Meteorol.*, 39, 437-445,  
655 10.1175/1520-0450(2000)039<0437:NWDSAI>2.0.CO;2, 2000.
- 656 Che, H., Xia, X., Zhu, J., Li, Z., Dubovik, O., Holben, B., Goloub, P., Chen, H.,  
657 Estelles, V., Cuevas-Agulló, E., Blarel, L., Wang, H., Zhao, H., Zhang, X., Wang, Y.,  
658 Sun, J., Tao, R., Zhang, X., and Shi, G.: Column aerosol optical properties and aerosol  
659 radiative forcing during a serious haze-fog month over North China Plain in 2013  
660 based on ground-based sunphotometer measurements, *Atmos. Chem. Phys.*, 14,  
661 2125-2138, 10.5194/acp-14-2125-2014, 2014.
- 662 Che, H. C., Zhang, X. Y., Wang, Y. Q., Zhang, L., Shen, X. J., Zhang, Y. M., Ma, Q. L.,  
663 Sun, J. Y., Zhang, Y. W., and Wang, T. T.: Characterization and parameterization of  
664 aerosol cloud condensation nuclei activation under different pollution conditions, *Sci.*  
665 *Rep.*, 6, 24497, 10.1038/srep24497, 2016.



- 666 Chen, Y., An, J. L., Wang, X. Q., Sun, Y. L., Wang, Z. F., and Duan, J.: Observation of  
667 wind shear during evening transition and an estimation of submicron aerosol  
668 concentrations in Beijing using a Doppler wind lidar, *J. Meteor. Res.*, 31, 350-362,  
669 10.1007/s13351-017-6036-3, 2017.
- 670 Chen, Y., An, J. L., Sun, Y. L., Wang, X. Q., Qu, Y., Zhang, J. W., Wang, Z. F., and  
671 Duan, J.: Nocturnal low-level winds and their impacts on particulate matter over the  
672 Beijing area, *Adv. Atmos. Sci.*, 35, 1455-1468, 10.1007/s00376-018-8022-9, 2018.
- 673 Cheng, X. L., Liu, X. M., Liu, Y. J., and Hu, F.: Characteristics of CO<sub>2</sub> concentration  
674 and flux in the Beijing urban area, *J. Geophys. Res.*, 10.1002/2017jd027409, 2018.
- 675 Dickerson, R. R.: The Impact of Aerosols on Solar Ultraviolet Radiation and  
676 Photochemical Smog, *Science*, 278, 827-830, 10.1126/science.278.5339.827, 1997.
- 677 Ding, A. J., Huang, X., Nie, W., Sun, J. N., Kerminen, V. M., Petäjä, T., Su, H., Cheng,  
678 Y. F., Yang, X. Q., Wang, M. H., Chi, X. G., Wang, J. P., Virkkula, A., Guo, W. D.,  
679 Yuan, J., Wang, S. Y., Zhang, R. J., Wu, Y. F., Song, Y., Zhu, T., Zilitinkevich, S.,  
680 Kulmala, M., and Fu, C. B.: Enhanced haze pollution by black carbon in megacities in  
681 China, *Geophys. Res. Lett.*, 43, 2873-2879, 10.1002/2016gl067745, 2016.
- 682 Emeis, S., Münkler, C., Vogt, S., Müller, W. J., and Schäfer, K.: Atmospheric  
683 boundary-layer structure from simultaneous SODAR, RASS, and ceilometer  
684 measurements, *Atmos. Environ.*, 38, 273-286, 10.1016/j.atmosenv.2003.09.054, 2004.
- 685 Farrugia, R. N.: The wind shear exponent in a Mediterranean island climate,  
686 *Renewable Energy*, 28, 647, 10.1016/S0960-1481(02)00066-6, 2003.
- 687 Flamant, C., Pelon, J., Flamant, P. H., and Durand, P.: Lidar determination of the  
688 entrainment zone thickness at the top of the unstable marine atmospheric boundary  
689 layer, *Boundary-Layer Meteorol.*, 83, 247-284, 1997.
- 690 Gao, Y., Zhang, M., Liu, Z., Wang, L., Wang, P., Xia, X., Tao, M., and Zhu, L.:  
691 Modeling the feedback between aerosol and meteorological variables in the  
692 atmospheric boundary layer during a severe fog-haze event over the North China  
693 Plain, *Atmos. Chem. Phys.*, 15, 4279-4295, 10.5194/acp-15-4279-2015, 2015.
- 694 Georgoulias, A. K., Papanastasiou, D. K., Melas, D., Amiridis, V., and Alexandri, G.:  
695 Statistical analysis of boundary layer heights in a suburban environment, *Meteorol.*  
696 *Atmos. Phys.*, 104, 103-111, 10.1007/s00703-009-0021-z, 2009.
- 697 Guinot, B., Roger, J. C., Cachier, H., Wang, P. C., Bai, J. H., and Yu, T.: Impact of  
698 vertical atmospheric structure on Beijing aerosol distribution, *Atmos. Environ.*, 40,  
699 5167-5180, 10.1016/j.atmosenv.2006.03.051, 2006.
- 700 Gunthe, S. S., Rose, D., Su, H., Garland, R. M., Achtert, P., Nowak, A., Wiedensohler,  
701 A., Kuwata, M., Takegawa, N., Kondo, Y., Hu, M., Shao, M., Zhu, T., Andreae, M. O.,  
702 and Pöschl, U.: Cloud condensation nuclei (CCN) from fresh and aged air pollution in  
703 the megacity region of Beijing, *Atmos. Chem. Phys.*, 11, 11023-11039,  
704 10.5194/acp-11-11023-2011, 2011.
- 705 Guo, J. P., Xia, F., Zhang, Y., Liu, H., Li, J., Lou, M. Y., He, J., Yan, Y., Wang, F., Min,  
706 M., and Zhai, P. M.: Impact of diurnal variability and meteorological factors on the  
707 PM<sub>2.5</sub> - AOD relationship: Implications for PM<sub>2.5</sub> remote sensing, *Environ. Pollut.*,  
708 221, 94-104, 10.1016/j.envpol.2016.11.043, 2017.
- 709 Halios, C. H., and Barlow, J. F.: Observations of the morning development of the  
710 urban boundary layer over London, UK, taken during the ACTUAL project,  
711 *Boundary-Layer Meteorol.*, 166, 395-422, 10.1007/s10546-017-0300-z, 2018.
- 712 Haman, C. L., Lefer, B., and Morris, G. A.: Seasonal variability in the diurnal  
713 evolution of the boundary layer in a near-coastal urban environment, *J. Atmos. Ocean.*  
714 *Technol.*, 29, 697-710, 10.1175/jtech-d-11-00114.1, 2012.
- 715 Han, S. Q., Bian, H., Tie, X. X., Xie, Y. Y., Sun, M. L., and Liu, A. X.: Impact of



- 716 nocturnal planetary boundary layer on urban air pollutants: measurements from a  
717 250-m tower over Tianjin, China, *J. Hazard Mater.*, 162, 264-269,  
718 10.1016/j.jhazmat.2008.05.056, 2009.
- 719 Han, S. Q., Hao, T. Y., Zhang, Y. F., Liu, J. L., Li, P. Y., Cai, Z. Y., Zhang, M., Wang,  
720 Q. L., and Zhang, H.: Vertical observation and analysis on rapid formation and  
721 evolutionary mechanisms of a prolonged haze episode over central-eastern China, *Sci.*  
722 *Total Environ.*, 616-617, 135-146, 10.1016/j.scitotenv.2017.10.278, 2018.
- 723 Hastie, D. R., Shepson, P. B., Sharma, S., and Schiff, H. I.: The influence of the  
724 nocturnal boundary layer on secondary trace species in the atmosphere at Dorset,  
725 Ontario, *Atmos. Environ.*, 27A, 533-541, 10.1016/0960-1686(93)90210-P, 1993.
- 726 Holmes, H. A., Sriramasamudram, J. K., Pardyjak, E. R., and Whiteman, C. D.:  
727 Turbulent fluxes and pollutant mixing during wintertime air pollution episodes in  
728 complex terrain, *Environ. Sci. Technol.*, 49, 13206-13214, 10.1021/acs.est.5b02616,  
729 2015.
- 730 Hu, X. M., Klein, P. M., Xue, M., Zhang, F. Q., Doughty, D. C., Forkel, R., Joseph, E.,  
731 and Fuentes, J. D.: Impact of the vertical mixing induced by low-level jets on  
732 boundary layer ozone concentration, *Atmos. Environ.*, 70, 123-130,  
733 10.1016/j.atmosenv.2012.12.046, 2013.
- 734 Hu, X. M., Ma, Z. Q., Lin, W. L., Zhang, H. L., Hu, J. L., Wang, Y., Xu, X. B.,  
735 Fuentes, J. D., and Xue, M.: Impact of the Loess Plateau on the atmospheric boundary  
736 layer structure and air quality in the North China Plain: a case study, *Sci. Total*  
737 *Environ.*, 499, 228-237, 10.1016/j.scitotenv.2014.08.053, 2014.
- 738 Huang, M., Gao, Z. Q., Miao, S. G., Chen, F., LeMone, M. A., Li, J., Hu, F., and  
739 Wang, L. L.: Estimate of boundary-layer depth over Beijing, China, using Doppler  
740 Lidar data during SURF-2015, *Boundary-Layer Meteorol.*, 162, 503-522,  
741 10.1007/s10546-016-0205-2, 2017.
- 742 Kotthaus, S., and Grimmond, C. S. B.: Energy exchange in a dense urban  
743 environment – Part I: Temporal variability of long-term observations in central  
744 London, *Urban Clim.*, 10, 261-280, 10.1016/j.uclim.2013.10.002, 2014.
- 745 Lee, X. H., Gao, Z. Q., Zhang, C. L., Chen, F., Hu, Y. Q., Jiang, W. M., Liu, S. H., Lu,  
746 L. H., Sun, J. L., Wang, J. M., Zeng, Z. H., Zhang, Q., Zhao, M., and Zhou, M. Y.:  
747 Priorities for boundary layer meteorology research in China, *Bull. Am. Meteorol. Soc.*,  
748 96, ES149-ES151, 10.1175/bams-d-14-00278.1, 2015.
- 749 Li, J., Sun, J. L., Zhou, M. Y., Cheng, Z. G., Li, Q. C., Cao, X. Y., and Zhang, J. J.:  
750 Observational analyses of dramatic developments of a severe air pollution event in the  
751 Beijing area, *Atmos. Chem. Phys.*, 18, 3919-3935, 10.5194/acp-18-3919-2018, 2018.
- 752 Li, X., Zhang, Q., Zhang, Y., Zhang, L., Wang, Y. X., Zhang, Q. Q., Li, M., Zheng, Y.  
753 X., Geng, G. N., Wallington, T. J., Han, W. J., Shen, W., and He, K. B.: Attribution of  
754 PM<sub>2.5</sub> exposure in Beijing–Tianjin–Hebei region to emissions: implication to control  
755 strategies, *Sci. Bull.*, 62, 957-964, 10.1016/j.scib.2017.06.005, 2017.
- 756 Li, Z. Q., Guo, J. P., Ding, A. J., Liao, H., Liu, J. J., Sun, Y. L., Wang, T. J., Xue, H.  
757 W., Zhang, H. S., and Zhu, B.: Aerosol and boundary-layer interactions and impact on  
758 air quality, *Natl. Sci. Rev.*, 4, 810-833, doi:<https://doi.org/10.1093/nsr/nwx117>, 2017.
- 759 Liu, C. W., Gao, Z. Q., Li, Y. B., Gao, C. Y., Su, Z. B., and Zhang, X. Y.: Surface  
760 energy budget observed at a winter wheat field site in the north China plain during a  
761 fog-haze event, *Boundary-Layer Meteorol.*, 10.1007/s10546-08-0407, 2018.
- 762 Liu, J. K., Gao, Z. Q., Wang, L. L., Li, Y. B., and Gao, C. Y.: The impact of  
763 urbanization on wind speed and surface aerodynamic characteristics in Beijing during  
764 1991–2011, *Meteorol. Atmos. Phys.*, 130, 311-324, 10.1007/s00703-017-0519-8,  
765 2017.



- 766 Liu, S. H., Liu, Z. X., Li, J., Wang, Y. C., Ma, Y. J., Sheng, L., Liu, H. P., Liang, F. M.,  
767 Xin, G. J., and Wang, J. H.: Numerical simulation for the coupling effect of local  
768 atmospheric circulations over the area of Beijing, Tianjin and Hebei Province, *Sci.*  
769 *China Ser. D*, 52, 382-392, 10.1007/s11430-009-0030-2, 2009.
- 770 Luan, T., Guo, X. L., Guo, L. J., and Zhang, T. H.: Quantifying the relationship  
771 between PM<sub>2.5</sub> concentration, visibility and planetary boundary layer height for  
772 long-lasting haze and fog-haze mixed events in Beijing, *Atmos. Chem. Phys.*, 18,  
773 203-225, 10.5194/acp-18-203-2018, 2018.
- 774 Mahrt, L., Sun, J. I., Blumen, W., Delany, T., and Oncley, S.: Nocturnal  
775 boundary-layer regimes, *Boundary-Layer Meteorol.*, 88, 255-278,  
776 10.1023/A:1001171313493, 1998.
- 777 Mahrt, L.: Stratified atmospheric boundary layers, *Boundary-Layer Meteorol.*, 90,  
778 375-396, 1999.
- 779 Mahrt, L., and Vickers, D.: Contrasting vertical structures of nocturnal boundary layers,  
780 *Boundary-Layer Meteorol.*, 105, 351-363, 10.1023/A:1019964720989, 2002.
- 781 Miao, S. G., Chen, F., Li, Q. C., and Fan, S. Y.: Impacts of urban processes and  
782 urbanization on summer precipitation: A case study of heavy rainfall in Beijing on 1  
783 August 2006, *J. Appl. Meteorol. Climatol.*, 50, 806-825, 10.1175/2010jamc2513.1,  
784 2011.
- 785 Miao, S. G., Dou, J. X., Chen, F., Li, J., and Li, A. G.: Analysis of observations on the  
786 urban surface energy balance in Beijing, *Sci. China Earth Sci.*, 55(11), 1881-1890,  
787 10.1007/s11430-012-4411-6, 2012.
- 788 Oke, T. R., Mills, G., Christen, A., and Voogt, J. A.: *Urban climates*, Cambridge  
789 University Press, Cambridge, 157pp, 2017.
- 790 Pearson, G., Davies, F., and Collier, C.: Remote sensing of the tropical rain forest  
791 boundary layer using pulsed Doppler lidar, *Atmos. Chem. Phys.*, 10, 5891-5901,  
792 2010.
- 793 Petäjä, T., Järvi, L., Kerminen, V. M., Ding, A. J., Sun, J. N., Nie, W., Kujansuu, J.,  
794 Virkkula, A., Yang, X. Q., Fu, C. B., Zilitinkevich, S., and Kulmala, M.: Enhanced air  
795 pollution via aerosol-boundary layer feedback in China, *Sci. Rep.*, 6, 18998,  
796 <https://doi.org/10.1038/srep18998>, 2016.
- 797 Ramanathan, V., Crutzen, P. J., Kiehl, J. T., and Rosenfeld, D.: Aerosols, climate, and  
798 the hydrological cycle, *Science*, 294, 2119-2126, 10.1126/science.1064034, 2001.
- 799 Salmond, J. A., and McKendry, I. G.: A review of turbulence in the very stable  
800 nocturnal boundary layer and its implications for air quality, *Prog. Phys. Geog.*, 29,  
801 171-188, 10.1191/0309133305pp442ra, 2005.
- 802 Stone, R. S., Anderson, G. P., Shettle, E. P., Andrews, E., Loukachine, K., Dutton, E.  
803 G., Schaaf, C., and Roman, M. O.: Radiative impact of boreal smoke in the Arctic:  
804 Observed and modeled, *J. Geophys. Res.*, 113, 10.1029/2007jd009657, 2008.
- 805 Stull, R. B.: *An Introduction to Boundary Layer Meteorology*, Atmospheric Sciences  
806 Library, 8, 89 pp., 1988.
- 807 Sun, Y., Song, T., Tang, G. Q., and Wang, Y. S.: The vertical distribution of PM<sub>2.5</sub> and  
808 boundary-layer structure during summer haze in Beijing, *Atmos. Environ.*, 74,  
809 413-421, 10.1016/j.atmosenv.2013.03.011, 2013.
- 810 Sun, Y. L., Jiang, Q., Wang, Z. F., Fu, P. Q., Li, J., Yang, T., and Yin, Y.: Investigation  
811 of the sources and evolution processes of severe haze pollution in Beijing in January  
812 2013, *Journal of Geophysical Research: Atmospheres*, 119, 4380-4398, 10.1002/  
813 2014.
- 814 Sun, Y. L., Wang, Z. F., Wild, O., Xu, W. Q., Chen, C., Fu, P. Q., Du, W., Zhou, L. B.,  
815 Zhang, Q., Han, T. T., Wang, Q. Q., Pan, X. L., Zheng, H. T., Li, J., Guo, X. F., Liu, J.



- 816 G., and Worsnop, D. R.: “APEC Blue”: Secondary aerosol reductions from emission  
817 controls in Beijing, *Sci. Rep.*, 6, 20668, 10.1038/srep20668, 2016.
- 818 Tucker, S. C., Senff, C. J., Weickmann, A. M., Brewer, W. A., Banta, R. M., Sandberg,  
819 S. P., Law, D. C., Hardesty, R. M.: Doppler lidar estimation of mixing height using  
820 turbulence, shear, and aerosol profiles, *J. Atmos. Ocean. Technol.*, 26(4): 673-688,  
821 2009.
- 822 Wang, J. D., Xing, J., Wang, S. X., and Hao, J. M.: The pathway of aerosol direct  
823 effects impact on air quality: a case study by using process analysis. In EGU General  
824 Assembly Conference Abstracts, 19, 8568, 2017.
- 825 Van Den Heever, S. C., and Cotton, W. R.: Urban aerosol impacts on downwind  
826 convective storms, *J. Appl. Meteorol. Climatol.*, 46, 828-850, 10.1175/jam2492.1,  
827 2007.
- 828 Wang, L. L., Li, D., Gao, Z. Q., Sun, T., Guo, X. F., and Bou-Zeid, E.: Turbulent  
829 transport of momentum and scalars above an urban canopy, *Boundary-Layer*  
830 *Meteorol.*, 150, 485-511, 10.1007/s10546-013-9877-z, 2014.
- 831 Wang, L. T., Wei, Z., Yang, J., Zhang, Y., Zhang, F. F., Su, J., Meng, C. C., and Zhang,  
832 Q.: The 2013 severe haze over southern Hebei, China: model evaluation, source  
833 apportionment, and policy implications, *Atmos. Chem. Phys.*, 14, 3151-3173,  
834 10.5194/acp-14-3151-2014, 2014.
- 835 Wang, X. R., Miao, S. G., Dou, J. X., Dong, P., and Wang, J. L.: Observation and  
836 analysis of the air pollution impacts on radiation balance of urban and suburb areas in  
837 Beijing, *Chinese J. Geophys. (in Chinese)*, 59(11), 3996-4006, 10.6038/cjg20161106,  
838 2016.
- 839 Wang, Y., Li, Z. Q., Zhang, Y., Wang, Q., and Ma, J. Z.: Impact of aerosols on  
840 radiation during a heavy haze event in Beijing, *IOP Conf. Ser.: Earth Environ. Sci.*, 17,  
841 012012, 10.1088/1755-1315/17/1/012012, 2014.
- 842 Xia, X. G., Li, Z. Q., Holben, B., Wang, P. C., Eck, T., Chen, H. B., Cribb, M., and  
843 Zhao, Y. X.: Aerosol optical properties and radiative effects in the Yangtze Delta  
844 region of China, *J. Geophys. Res.*, 112, 10.1029/2007jd008859, 2007.
- 845 Yang, T., Wang, Z. F., Zhang, W., Gbaguidi, A., Sugimoto, N., Wang, X. Q., Matsui, I.,  
846 and Sun, Y. L.: Technical note: Boundary layer height determination from lidar for  
847 improving air pollution episode modeling: development of new algorithm and  
848 evaluation, *Atmos. Chem. Phys.*, 17, 6215-6225, 10.5194/acp-17-6215-2017, 2017.
- 849 Ye, X. X., Song, Y., Cai, X. H., and Zhang, H. S.: Study on the synoptic flow patterns  
850 and boundary layer process of the severe haze events over the North China Plain in  
851 January 2013, *Atmos. Environ.*, 124, 129-145, 10.1016/j.atmosenv.2015.06.011, 2016.
- 852 Yang Y.J., Zheng, X.Y., Gao, Z. Q., Wang, H., Wang, T.J., Li, Y.B., Lau, G.I.N.C.,  
853 Yim, S. H.L.: Long-Term Trends of Persistent Synoptic Circulation Events in  
854 Planetary Boundary Layer and Their Relationships with Haze Pollution in Winter  
855 Half-Year over Eastern China, *J. Geophys. Res.*, doi: 10.1029/2018JD028982, 2018
- 856 Yu, H. B., Liu, S. C., and Dickinson, R. E.: Radiative effects of aerosols on the  
857 evolution of the atmospheric boundary layer, *J. Geophys. Res.*, 107,  
858 10.1029/2001jd000754, 2002.
- 859 Zhang, R. H., Li, Q., and Zhang, R. N.: Meteorological conditions for the persistent  
860 severe fog and haze event over eastern China in January 2013, *Science China Earth*  
861 *Sciences*, 57, 26-35, 10.1007/s11430-013-4774-3, 2014.
- 862 Zhang, X. Y., Sun, J. Y., Wang, Y. Q., Li, W. J., Zhang, Q., Wang, W. G., Quan, J. N.,  
863 Cao, G. L., Wang, J. Z., Yang, Y. Q., and Zhang, Y. M.: Factors contributing to haze  
864 and fog in china. *Chin. Sci. Bull.*, 58(13), 1178, doi: 10.1360/972013-150, 2013.
- 865 Zhang, X. Y., Zhong, J. T., Wang, J. Z., Wang, Y. Q., and Liu, Y. J.: The interdecadal



866 worsening of weather conditions affecting aerosol pollution in the Beijing area in  
867 relation to climate warming. Atmos. Chem. Phys., 18, 1–9.  
868 <https://doi.org/10.5194/acp-18-1-2018>, 2018.  
869 Zhao, X. J., Zhao, P. S., Xu, J., Meng, W., Pu, W. W., Dong, F., He, D., and Shi, Q. F.:  
870 Analysis of a winter regional haze event and its formation mechanism in the North  
871 China Plain, Atmos. Chem. Phys., 13, 5685–5696, 10.5194/acp-13-5685-2013, 2013.  
872 Zhong, J. T., Zhang, X. Y., Wang, Y. Q., Sun, J. Y., Zhang, Y. M., Wang, J. Z., Tan, K.  
873 Y., Shen, X. J., Che, H. C., Zhang, L., Zhang, Z. X., Qi, X. F., Zhao, H. R., Ren, S. X.,  
874 and Li, Y.: Relative contributions of boundary-layer meteorological factors to the  
875 explosive growth of PM<sub>2.5</sub> during the red-alert heavy pollution episodes in Beijing in  
876 December 2016, J. Meteor. Res., 31, 809–819, 10.1007/s13351-017-7088-0, 2017.  
877